

Quantum-critical continuum in magic-angle twisted bilayer graphene

Alexandre Jaoui^{1,*}, Ipsita Das¹, Giorgio Di Battista¹, Jaime Díez-Mérida¹, Xiaobo Lu¹, Kenji Watanabe², Takashi Taniguchi², Hiroaki Ishizuka^{3,4}, Leonid Levitov⁴ and Dmitri K. Efetov^{1,*}

1. ICFO - Institut de Ciencies Fotoniques, The Barcelona Institute of Science and Technology, Castelldefels, Barcelona, 08860, Spain.
2. National Institute of Material Sciences, 1-1 Namiki, Tsukuba, 305-0044, Japan.
3. Department of Physics, Tokyo Institute of Technology, Meguro, Tokyo, 152-8551, Japan.
4. Department of Physics, Massachusetts Institute of Technology, Cambridge MA 02139, USA.

*Correspondence to: alexandre.jaoui@icfo.eu and dmitri.efetov@icfo.eu.

Abstract: The flat bands of magic-angle twisted bilayer graphene (MATBG) host strongly-correlated electronic phases such as correlated insulators, superconductors and a ‘strange metal’ state. The latter state, believed to hold the key to a deeper understanding of the electronic properties of MATBG, is obscured by the abundance of phase transitions; so far, this state could not be unequivocally differentiated from a metal undergoing frequent electron-phonon collisions. We report on transport measurements in superconducting (SC) MATBG in which the correlated insulator states were suppressed by screening. The uninterrupted metallic ground state features a T -linear resistivity extending over three decades in temperature, from 40 mK to 20 K, spanning a broad range of dopings including those where a correlation-driven Fermi surface reconstruction occurs. This ‘strange-metal’ behavior is distinguished by Planckian scattering rates and a linear magneto-resistivity $\rho \propto B$. To the contrary, near charge neutrality or a fully-filled flat band, as well as for devices twisted away from the magic angle, the archetypal Fermi liquid behavior is recovered. Our measurements demonstrate the existence of a quantum-critical phase whose fluctuations dominate the metallic ground state. Further, a transition to the ‘strange metal’ is observed upon suppression of the SC order, which suggests an intimate relationship between quantum fluctuations and superconductivity in MATBG.

Conventional metals, in which electron interactions are described by Landau’s Fermi-liquid theory, feature a hallmark temperature-dependent resistivity $\rho \propto T^2$ and a $\rho \propto B^2$ magneto-resistivity [1]. However, a strikingly different behavior arises in the presence of strong electron correlations, where alongside superconductors, magnets and insulators, unusual ‘strange’ metal phases can survive down to $T \rightarrow 0$, as reported in cuprates [2], ruthenates [3], pnictides [4], heavy-fermion systems [5] and, very recently, in twisted di-chalcogenides [6]. Such ‘strange’ metal phases display the unique dependences $\rho(T) \propto T$ and $\rho(B) \propto B$ and are associated with ultra-fast carrier scattering governed by the universal Planckian dissipation rate $1/\tau = k_B T/\hbar$, with \hbar the reduced Planck’s constant and k_B the Boltzmann’s constant [7]. The observation of $\rho(T) \propto T$ down to $T \rightarrow 0$ signals the proximity to a quantum critical point (QCP) : the neighboring metallic ground state is dominated by inelastic scattering with electronic quantum-critical fluctuations. These fluctuations have been mostly related to magnetic ordering [8], yet purely nematic fluctuations were also reported [9]. Understanding the intricate relationship between quantum fluctuations, finite-temperature ‘strange’ metallicity and the exotic phase transitions found in a wide variety of strongly-correlated systems is a major conundrum in condensed matter physics

Early measurements in twisted bilayer graphene rotated by the magic angle of $\theta = 1.1^\circ$ (MATBG) [10] observed a metallic phase at temperatures $1 \text{ K} < T < 30 \text{ K}$ with a linear $\rho \propto T$ [11,12] and Planckian scattering rates in close proximity to correlated-insulating (CI) [13, 14, 15, 16, 17, 22] and superconducting (SC) phases [15, 18, 19, 20, 21] for electron filling factors of $\nu \sim \pm 2$ per moiré unit cell. First interpretations suggested a ‘strange-metal’ phase [11], drawing direct analogy to other strongly correlated systems [2]. Subsequently, however, it was proposed that a conventional electron-acoustic phonon scattering mechanism [23] above a characteristic Bloch-Grüneisen temperature T_{BG} (typically, exceeding a few kelvin), could also result in a similar behavior under favorable assumptions [12, 27]. An investigation of the $T \rightarrow 0$ regime of MATBG would allow to definitively differentiate between these distinct scenarios, yet, such studies have so far been impeded by the abundant low-temperature insulating and SC phase transitions.

This manuscript reports on comprehensive electronic transport measurements extending down to unprecedentedly low temperatures of $T \sim 40 \text{ mK}$, which firmly establishes the existence of a ‘strange’ metal phase. In order to reveal the low-temperature metallic states, we deliberately chose MATBG devices with ultra-close metallic screening layers and twist-angles that slightly deviate from 1.1° [20, 24]. In particular, we focus on device D1 with a twist-angle $\theta = 1.04^\circ$ and a screening layer spacing of $d = 9.5 \text{ nm}$ (inset Fig.1.a), which did not show correlated-insulating phases but still showed robust SC phases. We performed resistivity measurements for a broad parameter space of (n, T, B) with carrier density n tuned across the entire flat-band region, temperatures from $T = 40 \text{ mK}$ to $T = 100 \text{ K}$ and magnetic fields up to $B = 1 \text{ T}$ (see SI for more details). Our measurements confirm the existence of a T -linear resistivity in the center of the flat-bands above $T > 1 \text{ K}$, in agreement with previous results [11, 12], and firmly establish its uninterrupted continuation down to 40 mK , which cannot be explained by an electron-phonon mechanism. Further, we unveil another signature of the ‘strange’ metal state: a linear B -dependence of the resistivity. In contrast, we find a typical Fermi-liquid behavior $\rho \propto (T^2, B^2)$ in the vicinity of the band edges, and in twisted bilayer graphene (TBG) with twist-angles that strongly deviate from the magic-angle $\theta > 1.3^\circ$ (see SI for more details). Lastly, we demonstrate that the ‘strange’ metal state extends into the SC dome region after suppressing SC by a magnetic field. These observations establish the existence of a quantum-critical continuum and demonstrate a strong resemblance between MATBG and a variety of quantum-critical systems, pointing to an intricate relationship between electronic quantum fluctuations and SC/CI states. While recent findings of the isospin Pomeranchuk effect in MATBG [25, 26] point to soft spin and valley fluctuations as a driving mechanism of the low- T phase diagram, the nature of the quantum fluctuation in MATBG remains an open question.

Fig. 1.a shows the four-terminal resistivity ρ of device D1 as a function of the moiré band filling factor $\nu = n/n_0$ with $n_0 = 1/A_0$ (A_0 is the area of the moiré unit cell) for temperatures ranging from $T = 40 \text{ mK}$ up to $T = 20 \text{ K}$. We observe insulating behavior, i.e. an increasing resistivity when temperature is decreased, at electrostatic doping levels which correspond to the vicinity of the charge neutrality point (CNP) $\nu = 0$, for the fully-filled flat band $\nu = \pm 4$ and around $\nu = +3$. SC domes are found close to half-filling ($\nu = \pm 2$). By choosing a screening layer separation that is smaller than a typical Wannier orbital size of 15 nm [20] we were able to quench the correlated insulators at $\nu = \pm 2$ and leave the hole-doped region entirely metallic (apart from the SC dome). Clearly resolved is also the isospin Pomeranchuk effect, where especially the resistance peaks at $\nu = \pm 1$ are more pronounced at elevated T [25, 26]. The simplicity of the phase diagram of the hole-doped D1 allows for an in-depth study of the metallic ground state and its ties to the neighboring states. Similar datasets

measured on other devices, shown in the SI, draw a consistent picture of the metallic ground state.

We first discuss the temperature dependence of the resistivity and its evolution with the filling factor. A basic zero-order picture emerges from the (numerical) derivative $(\partial\rho/\partial T)_v$ shown in Fig. 1.b : it is roughly temperature independent in a wide range of filling factors and is weakly sensitive to doping. The details of this behavior are illustrated in Fig.1.c which present the resistivity vs. temperature for a variety of filling factors. Starting from the insulating regime at the CNP, metallicity is recovered at $v \sim -0.15$, which first shows a super-linear temperature dependence below $T < 15$ K, and then saturates into a linear dependence. With increased doping, the onset of the linear dependence is quickly shifted to lower temperatures. Starting from $v \sim 2$, the T -linear regime extends down to the base temperature and remains T -linear until a second super-linear regime is found for $v < -3.5$, which is only interrupted by a SC transition around half-filling.

We analyze the temperature dependence below $T < 10$ K by fitting the resistivity with $\rho(T) = \rho_0 + A_{T,\gamma}T^\gamma$, where the parameters $A_{T,\gamma}$ and γ define the prefactor and the exponent of the power-law T -dependence, and ρ_0 is the residual resistance at $T = 0$. Fig 1.d shows $(\rho(T) - \rho_0)$ on a log-log scale, which allows to trace $\rho(T)$ over more than three orders of magnitude down to milli Kelvin temperatures. We fit each curve with $A_{T,\gamma}T^\gamma$, which results in linear lines on the log-log plot, with a slope that is directly defined by $\gamma = \partial[\ln(\rho(T) - \rho_0)]/\partial[\ln(T)]$. In proximity of the CNP ($v = -0.2$) and of full filling ($v = -3.7$), we find a $\gamma = 2 \pm 0.1$ which results in a super-linear $\rho(T) \propto T^{2 \pm 0.1}$ dependence. However, for the filling factor range of $-3.5 < v < -2$ we find $\gamma = 1$, which gives rise to a strictly linear $\rho(T) \propto T$ dependence with an ultra-high filling dependent slope of $A_{T,1} > 0.3$ k Ω /K, which is shown in the inset of Fig.1.d. Strikingly the T -linear dependence extends without interruption from the base temperature of $T = 40$ mK to a temperature of $T \sim 10$ K, above which it saturates (see the SI for a discussion on the saturation upon reaching the Mott-Ioffe-Regel limit). The unique aspects of this ‘zero-temperature’ transition are discussed in detail below.

Can the observed linear dependence be explained by electron-phonon scattering? The electron-phonon mechanism yields a weak T -linear resistivity only above the Bloch-Grüneisen temperature which typically has values $T_{BG} > 10$ K, whereas below T_{BG} the T -dependence is superlinear, $\rho_{e-ph} \propto T^4$ [27]. The temperature of 40mK at which the T -linearity is observed in device D1 is three orders of magnitude lower than T_{BG} , and the observed slope of $A_{T,1} \sim 0.3$ k Ω /K is much higher than expected from an electron-phonon mechanism. Since T_{BG} is however proportional to the square root of n , $T_{BG} \propto \sqrt{n}$ [23], it has been suggested that near the CNP ($v = 0$) or Fermi energy resets at ($v = \pm 2$) [16], where n and T_{BG} become small, a $\rho_{e-ph} \propto T$ dependence with an enhanced slope can persist to temperatures as low as $T = 0.5$ K [12, 27]. This scenario is however inconsistent with our findings as we observe 1) a large interval of fillings where the low- T linear regime occurs, 2) the emergence of a T^2 -dependent resistivity of the same amplitude near the flat band edges, 3) the evolution of the prefactor $A_{T,\gamma}$ as a function of doping, which sharply increases for $v < -3$, as shown in the inset of Fig.1.d and 4) that devices with $\theta > 1.3^\circ$, which because of strongly increased band-widths host no signatures of correlations, also show no signs of a T -linear resistivity for $T \rightarrow 0$, and instead show a super-linear T^2 -dependence across the entire hole-doped band, as is worked out in the SI in more detail.

These findings are summarized in a schematic phase diagram in Fig.2.a, and are overall much better explained by a purely electronic phenomenon. The metallic ground state at the edges of the band is a Fermi liquid that displays a quadratic T^2 -dependence of resistivity. However, doping away from the band edges induces two ‘zero-temperature’ phase transitions, to a non-Fermi liquid state with a T -linear resistivity for filling factors $-3.5 < \nu < -2$. It is thus tempting to identify the latter state as a ‘strange’ metal above a quantum-critical continuum, wherein the finite- T metallic properties are dominated by critical fluctuations [4, 5, 28]. Support for this interpretation is offered by a comparison to the celebrated property of strange metals - a quasiparticle scattering time which is set by the Planckian limit $1/\tau = k_B T/\hbar$ regardless of the nature of the scattering events [30]. A rough estimate of the scattering rate (see SI) indicates that the inelastic T -linear resistivity is indeed consistent with Planckian dissipation, confirming previous reports [11]. Overall these findings resemble the T -linear resistivity observed in LSCO and Bi2201 [29] down to $T \rightarrow 0$, both at and away from a QCP, and are possibly associated with the reconstruction of the Fermi surface [16, 31, 32].

Additional evidence for the quantum-critical continuum is provided by the SC state close to $\nu \sim -2$, where we observe a recovery of the strange-metal phase upon suppression of the SC dome by a small perpendicular magnetic field $B_c \sim 300\text{mT}$ (Fig. 2.b). As shown in Fig.2.c for $T = 40\text{mK}$, above B_c the magnetoresistivity (MR) scales linearly $\rho(B) \propto B$ up to $B = 1\text{T}$. This allows us to evaluate the MR-corrected resistivity of the SC-suppressed state from the zero-field intercept of the linear B -dependence. Following this protocol for all temperatures we find the same ‘strange’ metal behavior $\rho(T) = \rho_0 + A_{T,1}T$ with a slope of $A_{T,1} \sim 0.3\text{k}\Omega/\text{K}$, for $T < T_c$ as for $T > T_c$ (Fig.2.b). A similar universal recovery of the ‘strange’ metal phase below the SC dome was previously reported in a wide variety of strongly-correlated systems [7, 29], in spite of the vast differences in their Fermi surfaces and their structural and magnetic properties.

Interestingly, the T -linear resistivity is accompanied by a B -linear magneto-resistivity also outside the SC dome. Such linear MR provides additional evidence for the existence of critical fluctuations that interact with the metallic ground state, and are characteristic of ‘strange’ metal phases in a multitude of systems including the cuprates [33, 34]. We illustrate the evolution of the MR across the band, where in Fig.3.a we show the (numerical) derivative $(\partial\rho/\partial B)_v$ and in Fig.3.b the resistivity vs. magnetic field for a variety of fillings. To quantitatively analyze the power-law scaling of the MR, we use a similar analysis as for the T -dependent resistivity, where we assume a B -dependence $\rho(B) = \rho_0 + A_{B,\gamma}B^\gamma$, where the parameters $A_{B,\gamma}$ and γ define the pre-factor and the exponent of the power-law B -dependence. We fit each B -field segment of the curves in Fig.3.b with $A_{B,\gamma}B^\gamma$, and plot the evolution of the corresponding logarithmic derivative $\gamma = \partial[\ln(\rho(B) - \rho_0)]/\partial[\ln(B)]$ as a function of B in Fig. 3.c. Overall we find a very similar picture to the temperature dependence. In proximity of the CNP ($\nu = -0.2$) and of full filling ($\nu = -3.7$), we find a $\gamma \sim 2$ and a $\rho(T) \propto B^2$ dependence for low B-fields $B < 0.4\text{T}$, which saturates at higher field. This saturation, as well as the saturation of the resistivity at high temperature are discussed in the SI. For the filling factor range of $-3.5 < \nu < -2$ we find a $\gamma \sim 1$, which gives rise to a linear $\rho(T) \propto B$ dependence with an ultra-high filling dependent slope of $A_{B,1} > 2\text{k}\Omega/\text{K}$ for $B > 0.2\text{T}$ (shown in the inset of Fig.1.d), but which saturates for $B \rightarrow 0$. We additionally show similar concomitant B -linear (up to 3T) and T -linear resistivities in another device with quasi-identical twist angle (only 0.01° apart) in the SI.

The observed linear MR is sharply distinct from previous reports of linear MR for graphene systems, which originate from purely classical effects [35, 36] and persist to $T = 300\text{K}$ and $B = 62\text{ T}$ [37]. Our MR is ~ 100 times stronger and is considerably more fragile, as it saturates near $B = 1\text{T}$ and is quickly suppressed at elevated T , as is illustrated in Fig. 3.d. As can be seen in Fig. 3.e, between $T = 40\text{ mK}$ and $T = 50\text{ K}$ the slope of the MR $A_{B,1}$ decreases ten-fold. In contrast, for devices with $\theta > 1.3^\circ$, we observe an almost absent magneto-resistivity (see SI). The identical scaling for the B - and T -dependences suggests the absence of an intrinsic energy scale in the ground state. We propose that it is dominated by scattering off quantum fluctuations, with a quasiparticle scattering rate which is given by the dominant energy scale $\hbar/\tau = \max\{\hbar/\tau_B, \hbar/\tau_T\} = \max\{\beta\mu_B B, \alpha k_B T\}$, where τ_B and τ_T are the magnetic and thermal scattering times, and μ_B is the Bohr magneton α and β are numerical factors. We estimate that at 1.9 K , $\tau_B = \tau_T$ at $B = 0.25\text{ T}$ (see SI for a detailed discussion), which corresponds exactly to the onset of the saturation observed in the low-field MR in Fig. 3.c. Hence, for $B \rightarrow 0$ we can conclude that the MR saturates because of finite temperature effects, similar to the case of LSCO [34]. To the contrary, the Ansatz proposed to describe transport relaxation rates of pnictides, cuprates, heavy fermions and twisted chalcogenides near a quantum critical point, $\hbar/\tau = \sqrt{(\alpha k_B T)^2 + (\beta\mu_B B)^2}$ [6, 33], fails to account for the MR of MATBG at finite temperatures.

These findings make a clear case that MATBG possesses a Planckian-limited T -linear resistivity that extends down to unprecedently low temperatures of $T \sim 40\text{ mK}$ and occurs alongside a quantum B -linear magnetoresistance. Such behavior is incompatible with a Fermi-liquid picture or dominant electron-phonon scattering. The Fermi-liquid behavior is observed throughout the entire moiré band at non-magic angles (as shown in a study of a variety of twist angles discussed in SI); in contrast, in MATBG it is pushed to the flat-band edges. We therefore conclude on the existence of a ‘strange’ metal phase above a quantum-critical continuum which is centered around the fillings where the Fermi surface reconstructs, and where quantum fluctuations dominate the metallic ground state of MATBG. We observe a clear connection between SC order and ‘strange’ metallicity, indicating that SC in MATBG emerges in a state dominated by quantum fluctuations. While the precise relationship between quantum fluctuations and phase transitions, as well as the microscopic nature of the fluctuations, remains an open problem, our work connects strongly correlated electronic moiré systems with the universality class of the quantum-critical matter.

References:

- [1] A. A. Abrikosov & I. M. Khalatnikov, Reports on Progress in Physics 22, 329 (1959).
- [2] C. Proust & L. Taillefer, Annual Review of Condensed Matter Physics 10, 409 (2019).
- [3] S. A. Grigera et al., Science 294, 329-332 (2001).
- [4] T. Shibauchi, et al. Ann. Rev. Condens. Matter Phys 5, 113 (2014).
- [5] H. V. Löhneysen et al., Physical Review Letters 72, 3262 (1994).
- [6] A. Ghiotto et al., arXiv:2103.09796 (2021).
- [7] J. A. N. Bruin et al., Science 339, 880 (2013).
- [8] O. Trovarelli et al., Physical Review Letters 85, 626 (2000).
- [9] S. Licciardello et al., Nature 567, 213-217 (2019).
- [10] R. Bistritzer & A. H. MacDonald, PNAS 108, 12233-12237 (2011).
- [11] Y. Cao et al., Physical Review Letters 124, 076801 (2020).
- [12] H. Polshyn et al., Nature Physics 15, 1011-1016 (2019).
- [13] Y. Cao et al., Nature 556, 80-84 (2018).
- [14] H. C. Po et al., Physical Review X 8, 031089 (2018).

- [15] X. Lu et al., *Nature* 574, 653-657 (2019).
- [16] U. Zondiner et al., *Nature* 582, 203-208 (2020).
- [17] D. Wong et al., *Nature* 582, 198-202 (2020).
- [18] Y. Cao, et al., *Nature* 556, 43-50 (2018).
- [19] M. Yankowitz et al., *Science* 363, 1059-1064 (2019).
- [20] P. Stepanov et al., *Nature* 583, 375-378 (2020).
- [21] Y. Saito et al., *Nature Physics* 16, 926-930 (2020).
- [22] A. L. Sharpe, E. J. Fox, et al., *Science* 365, 605-608 (2019).
- [23] D. K. Efetov & P. Kim, *Physical Review Letters* 105, 256805 (2010).
- [24] X. Liu et al., *Science* 371, 1261-1265 (2021).
- [25] Y. Saito et al., *Nature* 592, 220-224 (2021).
- [26] A. Rozen et al., *Nature* 592, 214–219 (2021).
- [27] F. Wu et al., *Phys. Rev. B* 99, 165112 (2019).
- [28] S. Paschen et al., *Nature* 432 (7019): 881–885
- [29] A. Legros et al., *Nature Physics* 15, 142-147 (2019).
- [30] J. Zaanen et al., *Nature* 430, 512–513 (2004).
- [31] R. Daou et al., *Nature Physics* 5, 31–34 (2009).
- [32] N. E. Hussey et al., *Journal of Physics: Conference Series* 449, 012004 (2013).
- [33] I. M. Hayes et al., *Nature Physics* 12, 916-919 (2016).
- [34] P. Giraldo-Gallo, J. A. Galvis, et al., *Science* 361, 479-481 (2019).
- [35] A. L. Friedman et al., *Nano Letters* 10, 3962-3965 (2010).
- [36] Z. M. Liao et al., *Europhysics Letters* 94, 57004 (2011).
- [37] F. Kisslinger et al., *Nature Physics* 11, 650-653 (2015).
- [38] J. R. Wallbank et al., *Nature Physics* 15, 32-36 (2019).
- [39] K. Kadowaki & S. B. Woods, *Solid State Communications* 58, 507 (1986).
- [40] X. Lin et al., *Science* 349, 945-948 (2015).
- [41] J. Custers et al., *Nature* 424, 524-527 (2003).
- [42] C. Collignon et al., *Physical Review X* 10, 031025 (2020).
- [43] N. Nagaosa & P. A. Lee, *Phys. Rev. Lett.* 64, 2450 (1990).
- [44] P.A. Lee, preprint: arXiv:2012.09339 (2020).
- [45] F. Wu et al., *Phys. Rev. B* 99, 165112 (2019).
- [46] H. Ishizuka, et al., preprint : arXiv:2011.01701 (2020).
- [47] M. Koshino et al., preprint : arXiv:1909.10786 (2019).
- [48] X. Cong et al., *Carbon* 149, 19-24 (2019).
- [49] J. M. Ziman, *Electrons and Phonons* Reprint ed. (Oxford Univ. Press, Oxford) (2001).
- [50] I. Yudhistira et al., *Phys. Rev. B* 99, 140302 (2019).
- [51] S. A. Hartnoll & A. P. Mackenzie, preprint arXiv:2107.07802 (2021).

Methods:

Screening layer fabrication process: The devices presented in this study were produced following the “cut-and-stack” method: a thin hBN flake is picked up with a propylene carbonate (PC) film, then placed on a 90 °C polydimethyl siloxane (PDMS) stamp. The hBN flake then allows to pick up a portion of a pre-cut monolayer graphene flake previously exfoliated mechanically on Si⁺⁺/SiO₂ (285nm) surface. Then, the remaining graphene sheet is rotated to a target angle usually around 1.1° - 1.15° and picked up by a hBN/graphene stack on PC (introduced previously). The resulting heterostructure is placed on top of another thin hBN flake (which thickness is chosen by optical contrast and further confirmed with atomic force microscopy measurements). Finally, the last layer of the heterostructure, sitting at the very bottom, is composed of a graphite flake (typically a few layer graphene thick) to create both a local back gate and a screening layer. The final stack is then placed on a target Si⁺⁺/SiO₂ (285 nm) wafer, where it is etched into a multiple Hall bar geometry using CHF₃/O₂ plasma and edge-coupled to Cr/Au (5/50 nm) metal contacts.

Transport measurements: Transport measurements were carried out in a dilution refrigerator (with base temperature 20-40mK) and an “Ice Oxford” VTI (with base temperature 1.6K). We used a standard low frequency lock-in technique using Stanford Research SR860 amplifiers with excitation frequency $f = 13.131$ Hz and Stanford Research SR560 pre-amplifiers. The back-gate voltage was controlled from Keithley 2400s voltage source-meters. DC voltage vs. DC excitation current measurements are also performed using SR560 low-noise DC voltage preamplifier in combination with a Keithley 2700 multimeter. In addition, we use a network of commercially available low-pass RC and RF filters to avoid any unwanted heating of the charge carriers. The measurement were realized for various excitation currents I (obtained by applying a tension to a $10\text{ M}\Omega$ resistor) ranging from ($I < 10\text{ nA}$) not to break the SC state and up to $I = 200\text{ nA}$ (to enhance the signal in the metallic phase), with a special attention given to ensure consistency between datasets. All in-field measurements reported in this work were realized with an applied out-of-plane magnetic field.

Acknowledgements:

We are grateful for fruitful discussions with Allan MacDonald, Pablo Jarillo-Herrero and Piers Coleman. D.K.E. acknowledges support from the Ministry of Economy and Competitiveness of Spain through the “Severo Ochoa” program for Centres of Excellence in R&D (SE5-0522), Fundació Privada Cellex, Fundació Privada Mir-Puig, the Generalitat de Catalunya through the CERCA program and funding from the European Research Council (ERC) under the European Union’s Horizon 2020 research and innovation programme (grant agreement No. 852927). L.L. acknowledges support from the Science and Technology Center for Integrated Quantum Materials, NSF Grant No. DMR-1231319; and Army Research Office Grant W911NF-18-1-0116. J.D. acknowledges support from the INPhINIT ‘la Caixa’ Foundation (ID 100010434) fellowship programme (LCF/BQ/DI19/11730021). G.d.B. acknowledges funding from the “Presidencia de la Agencia Estatal de Investigación” within the “Convocatoria de tramitación anticipada, correspondiente al año 2019, de las ayudas para contratos predoctorales (Ref. PRE2019-088487) para la formación de doctores contemplada en el Subprograma Estatal de Formación del Programa Estatal de Promoción del Talento y su Empleabilidad en I+D+i, en el marco del Plan Estatal de Investigación Científica y Técnica y de Innovación 2017-2020, cofinanciado por el Fondo Social Europeo. I.D. acknowledges the support from INphINIT “La Caixa” (ID 100010434) fellowship program (LCF/BQ/DI19/11730030).

Author contributions:

D.K.E. and X.L. conceived and designed the experiments; I.D., G.d.B., J.D-M. and X.L. fabricated the devices; I. D., A.J., G.d.B., J.D-M. and X.L. performed the measurements; A.J. analyzed the data; A.J., H.I. and L.L. performed the theoretical modeling; T.T. and K.W. contributed materials; D.K.E. supported the experiments; A.J. and D.K.E. wrote the paper.

Supplementary Information is available for this paper.

Correspondence and requests for materials should be addressed to D.K.E.

Reprints and permissions information is available.

Competing financial and non-Financial interests: The authors declare no competing financial and non-financial interests.

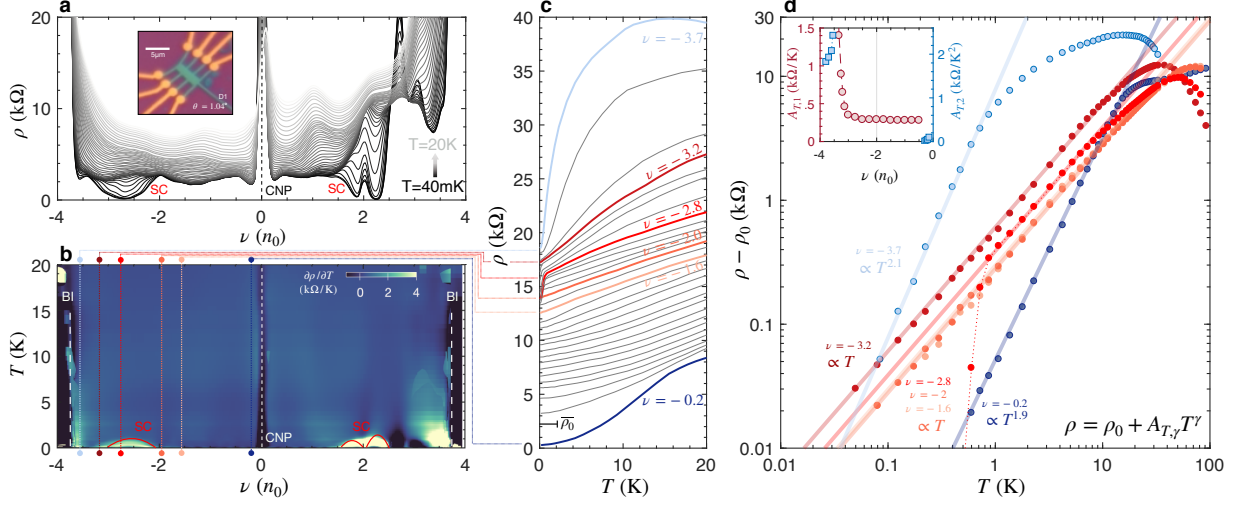


Fig. 1. Temperature dependence of the resistivity of hole-doped MATBG. **a** Resistivity ρ of device D1 ($\theta = 1.04^\circ$) as a function of the filling factor ν for successive temperatures ranging from $T = 40$ mK to $T = 20$ K. The charge neutrality point (CNP), band insulators (BI) and the SC domes are highlighted. Away from these regions, a metallic ground state is observed. Inset shows an optical image of the Hall bar device in which a four terminal geometry is used to measure ρ . **b** Map of $\partial\rho/\partial T$ vs. (ν, T) in D1. The SC, BI and CNP regions are emphasized. Vertical dotted lines represent the line cuts which are highlighted in the next sub-figure. **c** Temperature dependence of the resistivity for successive filling of the flat band from near CNP (bottom) to near full-filling (top). Curves are shifted for clarity and the typical residual $T \rightarrow 0$ resistivity $\bar{\rho}_0$ is shown. The low- T resistivity evolves from a super-linear T -dependence at the band edges, to a T -linear dependence in its center. **d** Log-log plot $\rho(T) - \rho_0$ vs. T for the highlighted filling factors in c. Power law fits of the low- T dependence are shown by straight lines. An evolution from a quadratic $\rho \propto T^2$ dependence near CNP and full-filling, to a linear $\rho \propto T$ dependence inside the flat-band region is seen. Inset shows the evolution of the prefactor $A_{T,\gamma}$ upon doping both for the linear-in- T resistivity (left y-axis) and the T -square resistivity (right y-axis).

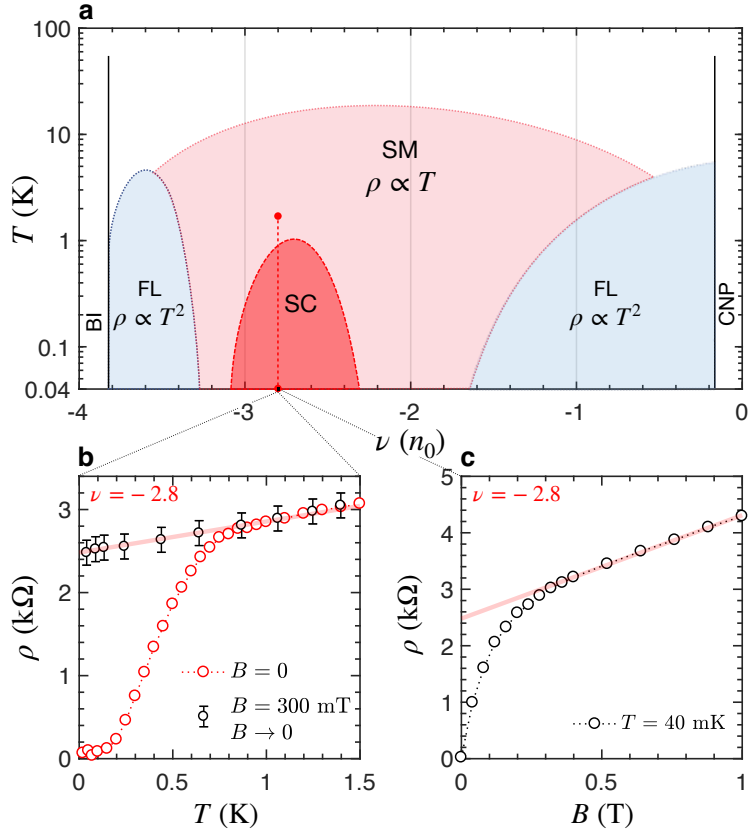


Fig. 2. Quantum critical continuum. **a** Schematic representation of the (ν, T) phase diagram of hole-doped MATBG. The superconducting dome is enclosed in a ‘strange’ metal region which is dominated by quantum fluctuations. The canonical Fermi liquid behavior is recovered near the boundary of the flat-band region. **b** $\rho(T)$ for $B = 0$ across the SC phase transition at $\nu = -2.8$, and the in-field corrected $\rho(T)$ for the critical field $B_c = 300$ mT. After suppression of the SC order, the uncovered metallic state is a ‘strange’ metal. **c** Evolution of the resistivity at $\nu = -2.8$ and $T = 40$ mK vs. B . The suppression of the SC order leads to a sharp increase of the resistivity, and is followed by a linear MR up to $B = 1$ T. The linear MR is highlighted by a solid red line.

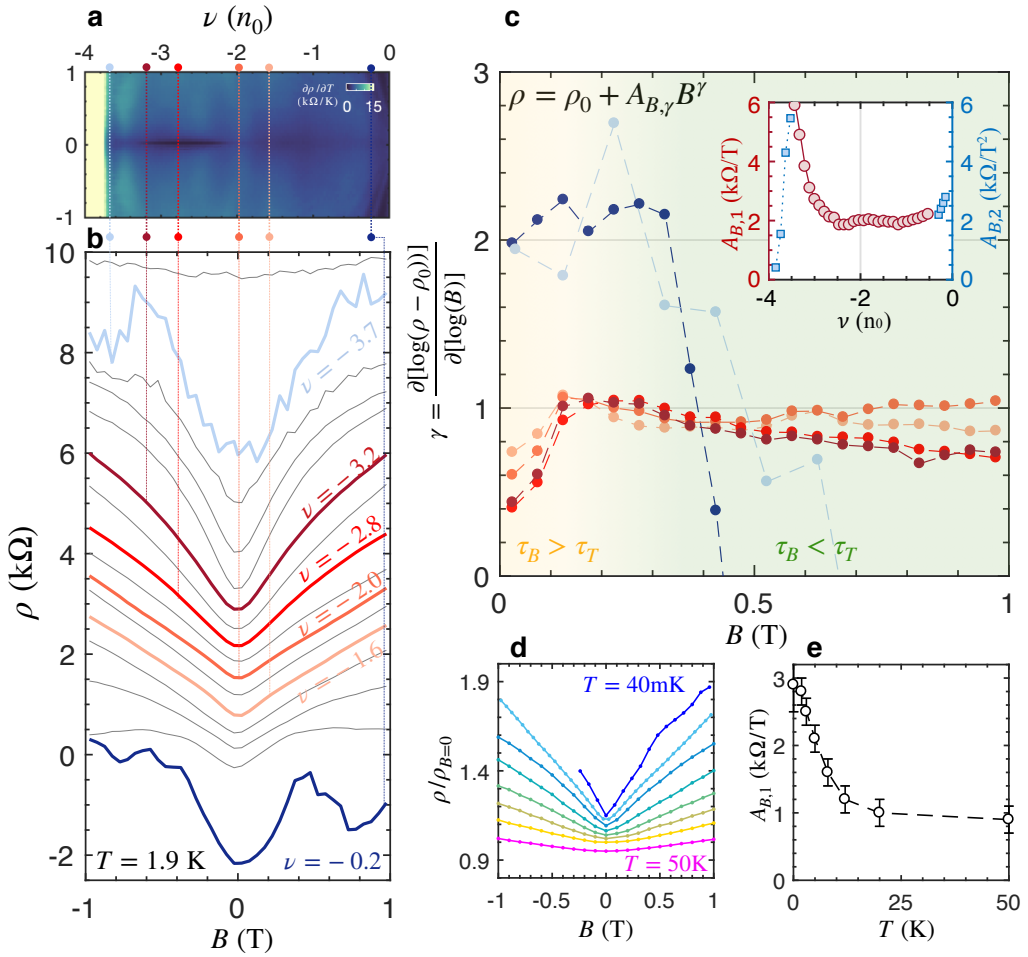


Fig. 3. Magnetic field dependence of the resistivity of hole-doped MATBG. **a** Map of $\partial\rho/\partial B$ as a function of (ν, B) . **b** Resistivity ρ as a function of magnetic field B for several filling factors (matching those detailed for the T -dependence in Fig. 1). **c** Shows the logarithmic derivative $\gamma = \partial[\ln(\rho(B) - \rho_0)]/\partial[\ln(B)]$ vs. B for the highlighted filling factors. A B -linear MR is found in the ‘strange’ metal phase in the band center, while a Fermi liquid-like B^2 -dependence prevails at the band edges. A saturation is seen at low field $B < 0.2$ T, which marks the crossover from thermal and magnetic dominated scattering times $\tau_T = \tau_B$. Inset shows the evolution of the linear and quadratic prefactors $A_{B,\gamma}$ upon doping. **d** Plots of $\rho(B)/\rho_{B=0}$ vs. B for different temperatures from $T = 40$ mK to $T = 50$ K. Curves are shifted for clarity. The linear magnetoresistance is suppressed upon increasing temperature. **e** Shows the slopes $A_{B,1}$ as extracted from d, as a function of T .

Supplementary Information: Quantum-critical continuum in magic-angle twisted bilayer graphene

Alexandre Jaoui^{1,*}, Ipsita Das¹, Giorgio Di Battista¹, Jaime Díez-Mérida¹, Xiaobo Lu¹, Kenji Watanabe², Takashi Taniguchi², Hiroaki Ishizuka^{3,4}, Leonid Levitov⁴ and Dmitri K. Efetov^{1,*}

1. ICFO - Institut de Ciencies Fotoniques, The Barcelona Institute of Science and Technology, Castelldefels, Barcelona, 08860, Spain.
2. National Institute of Material Sciences, 1-1 Namiki, Tsukuba, 305-0044, Japan.
3. Department of Physics, Tokyo Institute of Technology, Meguro, Tokyo, 152-8551, Japan.
4. Department of Physics, Massachusetts Institute of Technology, Cambridge MA 02139, USA.

*Correspondence to: alexandre.jaoui@icfo.eu and dmitri.efetov@icfo.eu.

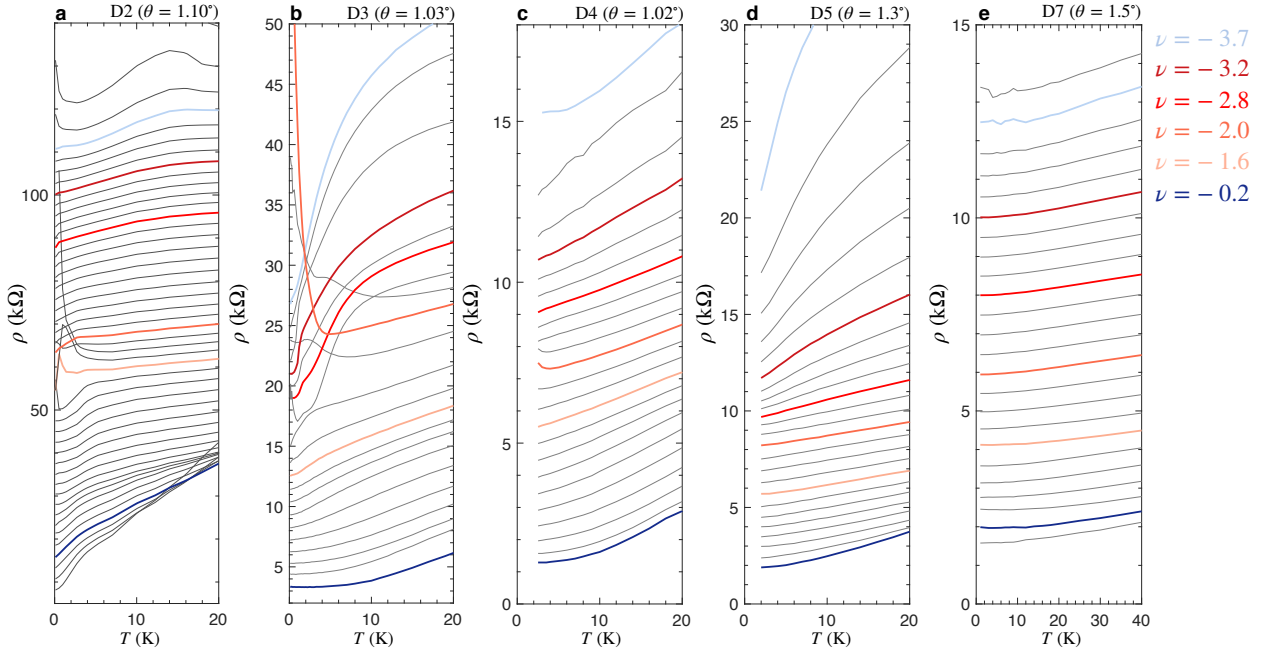
A. Table of studied devices

Device	Twist angle θ (°)	Width x Length (μm^2)
D1	1.04	3x2
D2	1.10	2.5x3
D3	1.03	2.9x3.6
D4	1.02	-
D5	1.3	3x3.5
D6	1.4	1.8x2.8
D7	1.5	1.4x7.4
D8	1.05	1.8x10.4

Supplementary Table S1: Geometry of the various devices discussed in this study.

B. Extended temperature dependent data of studied devices

Supplementary Fig.S1 shows the resistivity vs. temperature for several devices with various twist angles around the magic angle, D2 ($\theta = 1.10^\circ$), D3 ($\theta = 1.03^\circ$), D4 ($\theta = 1.02^\circ$), D5 ($\theta = 1.3^\circ$) and D7 ($\theta = 1.5^\circ$) respectively in subplots a,b,c,d and e. The dimensions of the devices are presented in Supplementary Table S1. Devices D2 and D3 show both SC and CI states and overall confirm our conclusions drawn on device D1: the resistivity scales super-linearly with temperature near the CNP, evolves into a T -linear term in the core of the flat band (although here interrupted at low- T by several phase transitions) before recovering Fermi liquid behavior near full-filling of the flat-band. Similar behavior, although not tracked below 2 K, is found in D4 and D5. On the contrary, device D7 with a twist-angle far from the magic angle shows no evidence of low- T linear resistivity. Device D6 shows similar ρ vs. T as device D7: a super-linear (quadratic) temperature dependence across the entire hole-doped flat-band, and is discussed in more detail in Fig. S2. We add that device D2 further shows a T^2 -dependent resistivity for $T > 20\text{K}$, reminiscent of reports on hBN-graphene hetero-structures, in which this quadratic resistance was associated with abundant electron-electron Umklapp processes [38].



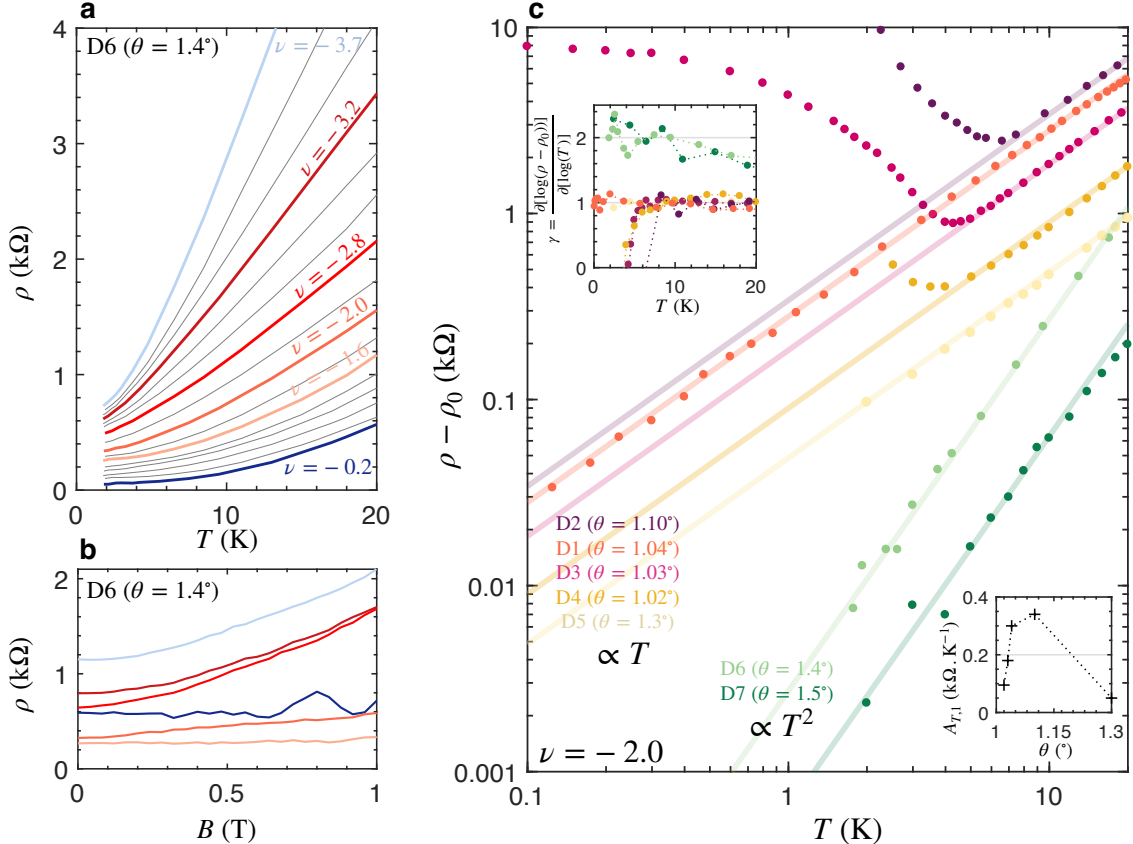
Supplementary Figure S1: Evolution of the resistivity of various twisted bilayer graphene devices both close to the magic angle and away from the magic angle. The highlighted filling factors are those discussed on device D1 in the main text. While ‘strange’ metal behavior, i.e. a linear-in- T resistivity is seen in D3, D4 and D5, device D7 shows only super-linear temperature dependence across the entire flat band.

C. Vanishing ‘strange’ metal phases in non-magic-angle devices.

Our report makes a convincing case that strong correlations in the flat-bands of MATBG give rise to quantum criticality. To check their intricate connection, we explore in detail devices with twist-angles that deviate from the magic angle (presented above). These devices have much weaker or absent correlations due to strongly increased band-widths. We find that the transport properties of such devices do not show signs of quantum-critical behavior, as it is highlighted in Fig. S2.a and b, which examine both the temperature and field dependences of device D6 with a twist angle of $\theta = 1.4^\circ$. These show $\rho(T)$ and $\rho(B)$ traces for the same filling factors as previously discussed for device D1. In stark contrast to device D1, we do not observe any sign of a linear-in- T and linear-in- B resistivity. Instead we find a super-linear temperature dependence across the entire hole-doped band, and an almost absent magneto-resistivity, which only shows a very weak super-linear dependence for $\nu < -2.8$. To highlight the dependence of quantum critical transport on the strength of the correlations, we examine a variety of devices D1 to D7 with different twist angles from $\theta = 1.02^\circ$ to 1.5° in Fig. S2.c. Similarly to what we have reported in Fig. 1.d., the resistivity of all devices is shown on a log-log scale as $(\rho(T) - \rho_0)$ for a filling of $\nu = -2$. We notice that devices D1 to D5, which are close to the magic angle, all show linear-in- T resistivity below $T < 20$ K.

While this resistivity scales linearly down to the lowest temperatures $T = 40$ mK in D1, it is interrupted by a metal-insulator transition in most other devices. The evolution of the slope $A_{T,1}$ with the twist angle is shown in the bottom inset of figure S2.c. $A_{T,1}$ peaks around the magic angle $\theta = 1.10^\circ$ at a value of 0.35 kΩ/K. This angle-dependent slope is in agreement with previous reports [11,12]. On the other hand, the devices twisted further away from the magic angle show a T^2 -dependence, i.e. Fermi liquid behavior. This evolution of the low-

temperature dependence of the resistivity at half-filling $\nu = -2$, from T -linear in devices close to the magic angle to a T^2 at larger twist angles is further clarified by the evolution of the logarithmic derivative of the inelastic resistivity $\gamma = \partial[\ln(\rho - \rho_0)]/\partial[\ln(T)]$ as a function of temperature in the top inset of Fig. S2.c. Additionally, the prefactor of the T^2 term (putative y -axis intercept in a log-log scale) decreases as the device is twisted away from the magic angle. In the Fermi liquid picture, $\rho(T) = \rho_0 + A_{T,2}T^2$ and $A_{T,2} \propto 1/E_F^2$ (as well as the electronic specific heat) are enhanced by electronic correlations, as described through the Kadowaki-Woods ratio [39,40]. This suggests that electronic correlations in the Fermi-liquid ground state are also enhanced near the magic angle.



Supplementary Figure S2: **a** Temperature dependence of the resistivity of device D6 ($\theta = 1.4^\circ$) for the filling factors discussed for device D1 in Fig. 1 and Fig. 3 of the manuscript. The low-temperature dependence remains super-linear over the whole flat-band region. **b** Magneto-resistivity of device D6 for the aforementioned filling factors. The MR vanishes or shows weak and non-linear B-dependence, in stark contrast with that of device D1. **c** Log-log graph of $(\rho(T) - \rho_0)$ as a function of T for devices D1 to D7 (sorted by increasing twist angle) at filling $\nu = -2$. The devices are presented in the supplementary table 1. Devices D1 to D5 display T -linear resistivity below $T < 20$ K. The specificity of device D1, i.e. its CI state is extinct due to screening, is illustrated here. On the contrary, devices D6 and D7 with twist angles the furthest away from the magic angle, show a low- T T^2 -dependent resistivity. Top inset underlines the power law dependence from the temperature logarithmic derivative $\gamma = \partial[\ln(\rho(T) - \rho_0)]/\partial[\ln(T)]$. The evolution of the slope $A_{T,1}$ as a function of twist angle is shown in the bottom inset.

D. Planckian dissipation

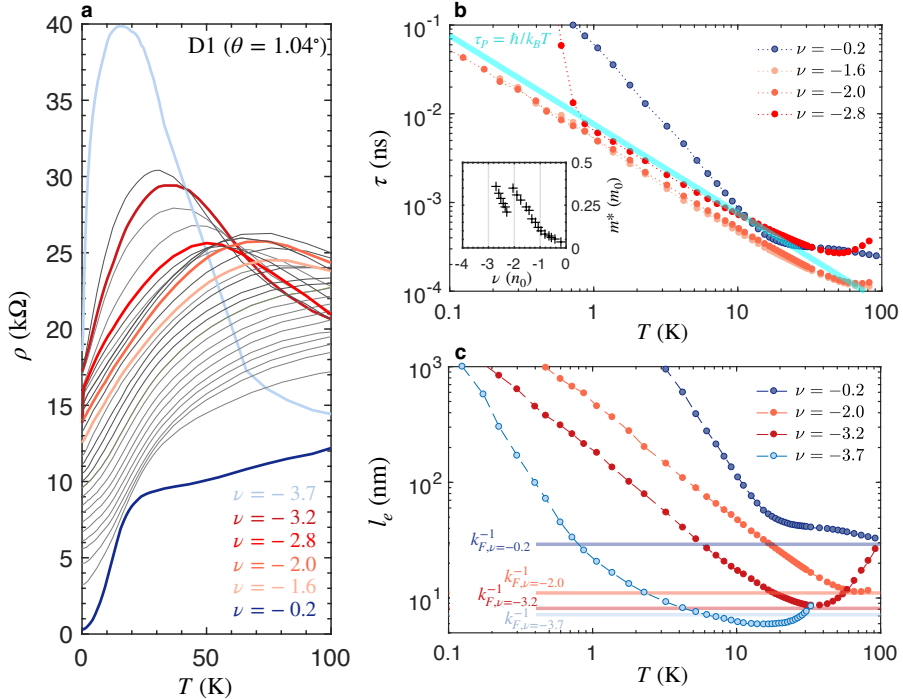
Supplementary Fig.S3.a shows the resistivity of the device D1, which is extensively discussed in this manuscript, at elevated temperatures from up to $T = 100\text{K}$. As mentioned in the main text, the resistivity displays a maximum at a finite temperature which is shifted to lower T with increasing filling of the electronic flat band. This result is in good agreement with the previous reports on MATBG where it was associated with thermal activation of higher energy bands [12].

In the Drude picture, the measured resistivity ρ is related to the scattering time of electrons (τ_e) and holes (τ_h) (with densities n and p , respectively) and their masses (m_e^* and m_h^* , respectively) by Eq.(S1):

$$\rho^{-1} = e^2 \left(\frac{n\tau_e}{m_e^*} + \frac{p\tau_h}{m_h^*} \right) \quad (\text{S1})$$

Here, for electrostatic hole doping, we make the assumption that the electronic density is given by the doping n . The inelastic scattering time is then given by the equation Eq.(S1) (see Ref [51] for an in-depth discussion on the relevant scattering rate which is to be evaluated).

$$\tau = \frac{\left(\frac{1}{\rho - \rho_0}\right)m^*}{ne^2} \quad (\text{S2})$$



Supplementary Figure S3: **a** Evolution of the resistivity of device D1 up to 100 K. **b** Evolution of the inelastic scattering time with temperature as evaluated from the Drude formula for the highlighted filling factors at which we could determine the effective mass of the carriers m^* and the carrier density n from a study of the Shubnikov de Haas effect. The inelastic scattering rate associated with the T -linear resistivity matches the Planckian scattering rate. A mismatch is expected from our crude approximation of an isotropic Fermi surface which contrasts with the peculiar filling of the flat band [16]. **c** Evolution of the electronic mean free path with

temperature. The saturation is observed when $l_e \sim 1/k_F$ i.e. when the system reaches the Mott-Ioffe-Regel limit.

To determine τ we obtain the requisite m^* of the quasiparticles from temperature dependent quantum oscillations in B -field, as shown in the inset of Fig. S3.b. We further use the linear $\rho(T)$ traces from Fig.1.d. of the main manuscript where we find ultra-steep slopes with $A_{T,1} = 0.3 \text{ k}\Omega/\text{K}$ for most filling factors. Fig. S3.b. shows the extracted Drude inelastic scattering times vs. temperature for several filling factors, and compares these with the temperature dependence of the Planckian scattering time. We find that $\tau \sim \hbar/k_B T$ for most filling factors where $\rho(T) \propto T$, which firmly confirms that the ‘strange’ metal phase of MATBG is set by the universal Planckian limit [11]. Consistent with this finding, we also find that for filling factors where a Fermi liquid prevails, i.e. $\nu = -0.2$, the scattering times are much bigger than the Planckian limit, $\tau > \hbar/k_B T$. Interestingly, for one filling factor, $\nu \sim -3.5$, we find a diverging slope $A_{T,1}$ which is enhanced tenfold (as can be seen in the inset of Fig.1.d). While for this filling m^* could not be directly determined due to the absence of clear quantum oscillations, upon assuming that the scattering rate across the ‘strange’ metal phase remains Planckian, the increase of $A_{T,1}$ translates into a steep increase of $m^* \propto A_{T,1}$. Such a sharp enhancement of the effective mass in the direct vicinity of a QCP has been previously reported in f -electron systems [41].

E. Saturation of resistivity at the Mott-Ioffe-Regel limit

Similarly to the scattering rate, the Drude model allows us to evaluate the inelastic mean-free-path l_e , given by the Eq.(S3) and shown in Fig.S3.c vs. temperature.

$$l_e = \left(\frac{\hbar}{e^2} \right) \left(\frac{1}{\rho - \rho_0} \right) \sqrt{\frac{4\pi}{n}} \quad (\text{S3})$$

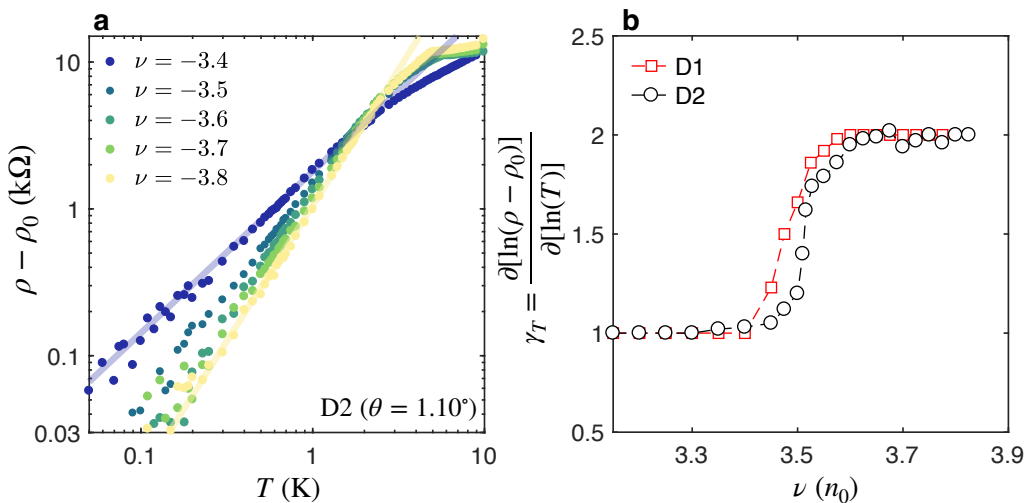
The Mott-Ioffe-Regel limit corresponds to the crossover from coherent to incoherent quasiparticle transport and is reached when their mean-free-path falls below any conceivable length scale of the system ($l_e < a, k_F^{-1}$) where a is the lattice constant. Our investigation of MATBG are limited to doping levels such that $k_F^{-1} > a$. We find that l_e decreases with temperature and saturates at $1/k_F$. We argue that the resistivity saturates when the electronic mean-free-path becomes comparable with the Fermi wavelength $l_e \sim 1/k_F$, i.e. upon reaching the Mott-Ioffe-Regel limit which separates coherent and incoherent quasiparticle transport regimes. At even higher temperatures, weakly resistive higher-energy electronic bands become thermally populated [12] and the resistivity decreases. Interestingly our findings comply with the Mott-Ioffe-Regel bound even though the scattering rate is of the order of the Planckian dissipation rate and the Fermi velocity is small. In contrast, apparent crossing of the Mott-Ioffe-Regel limit associated with non-saturating resistivity have been reported in cuprates [32] and non-degenerate ‘strange’ metals [42]. This picture may also explain a high field saturation of the magneto-resistivity in Fig. 3.c. of the main text, which is typically found around $B = 1\text{ T}$. For the case of $B = 1\text{ T}$, the value of the magnetic field matches the temperature of $T \sim 10\text{ K}$, which is the temperature for which the Mott-Ioffe-Regel limit is reached for $B = 0$. This firmly establishes that the saturation of the resistivity in (ν, B, T) is in agreement with $l_e \sim 1/k_F$. In comparison, the linear MR of other ‘strange’ metals does not usually saturate [33,34].

F. Finite temperature saturation of the magneto-resistivity

While the similarities in the T and B dependences are striking, there are also subtle differences. The B -linear MR does not extend down to the lowest excitations and saturates at finite temperatures below $B < 0.2$ T, which is highlighted in Fig.3.c of the main text. To understand the origin of this saturation, we consider the quasiparticle scattering rate. We define two scattering times: τ_B defined by $\hbar/\tau_B = \beta\mu_B B$ and its thermal counterpart τ_T : $\hbar/\tau_T = \alpha k_B T$ where μ_B is the Bohr magneton α and β are numerical factors. In the Drude model, the ratio B/T is given by $\tau_T/\tau_B = \beta\mu_B B/\alpha k_B T = A_{B,1}/A_{T,1}(B/T)$. For the case of $\nu = -2$, and $T = 1.9$ K presented in Fig.3.c, we obtain a slope of $A_{T,1} = 0.28$ k Ω /K and $A_{B,1} = 2.1$ k Ω /T (from Fig.1.d and Fig.3.e respectively). From this we can estimate that at 1.9 K, $\tau_B = \tau_T$ at $B = 0.25$ T, which corresponds exactly to the onset of the saturation observed in the low field MR, and hence, for $B \rightarrow 0$ we can conclude that the MR saturates at low fields because of finite temperature effects.

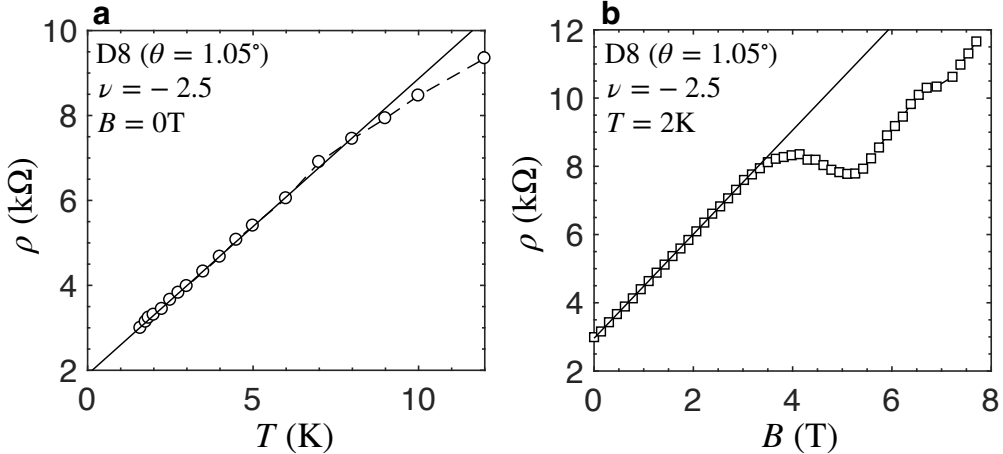
G. Evolution from ‘strange’ metal to Fermi liquid near full-filling

Supplementary Fig.S4.a shows the resistivity $\rho(T) - \rho_0$ vs. T on a log-log scale for device D2 with twist angle $\theta = 1.10^\circ$. The residual term ρ_0 was determined by fitting the resistivity $\rho = \rho_0 + A_{T,\gamma}T^\gamma$ for $T < 10$ K. The evolution of the slope (in a logarithmic scale) highlights the evolution from T -linear to T -quadratic upon increasing the filling of the flat band from $\nu = -3.4$ to $\nu = -3.8$. The evolution from the ‘strange’ metal behavior to the Fermi liquid behavior upon electrostatic doping is further underlined by the study of the evolution of the logarithmic derivative $\gamma = \partial[\ln(\rho - \rho_0)]/\partial[\ln(T)]$ for $T < 5$ K in Fig.S4.b. A clear crossover from $\gamma = 1$ to $\gamma = 2$ near $\nu = -3.5$ is seen in both devices D1 (raw data featured in the main text) and D2. The ‘zero’-temperature phase transition from a ‘strange’ metal to a canonical Fermi liquid is thus seen in both these superconducting devices.



Supplementary Figure S4: **a** Evolution of the resistivity of device D2 ($\theta = 1.10^\circ$) plotted as $\rho(T) - \rho_0$ vs. temperature on a log-log scale for different filling factors. A clear evolution from a T -linear to a T -quadratic dependence is seen. **b** The logarithmic derivative γ as a function of filling factor, shows a clear crossover from $\gamma = 1$ to $\gamma = 2$ near $\nu = -3.5$, for both devices D1 and D2.

H. Additional linear magnetoresistance data



Supplementary Figure S5: **a** Evolution of the resistivity of device D8 ($\theta = 1.05^\circ$) with temperature near half-filling ($\nu = -2.5$). **b** Evolution of the resistivity of device D8 ($\theta = 1.05^\circ$) with magnetic field at the same filling factor. The B -linear resistivity extends here up to 3 T.

We show both the temperature and magnetic field dependences of the resistivity of device D8 ($\theta = 1.05^\circ$), near half-filling of the flat-band ($\nu = -2.5$) in Fig. S5.a and S5.b respectively. This device, with an almost identical twist angle as device D1, also shows concomitant linear-in- T and linear-in- B resistivities near half-filling of the flat-band. The B -linear resistivity extends here up to ~ 3 T, making it more robust than in device D1.

I. Survey of theoretical models of electron transport discussed in the main text

In this section we summarize the results for the theoretical models of transport discussed in the main text, focusing on their predictions for the T -dependent resistivity. The predictions of the conventional quasiparticle scattering mechanisms - electron-phonon and electron-electron - strongly differ from the measured T -dependence. The Planckian dissipation mechanism, which is a general name for the mechanisms invoking carrier scattering by critical fluctuations, appears to be in a qualitative agreement with the observed linear- T scaling and the measured $\partial\rho/\partial T$ values.

As a quick summary, the coupling between electrons and acoustic phonons gives rise to a temperature-dependent scattering with a linear T -dependence above the Bloch-Grüneisen temperature $T_{BG} = sk_F$, where s is sound velocity. For typical k_F values in MATBG flat bands the temperature T_{BG} is on the order of a few kelvin. At temperatures $T < T_{BG}$ the predicted T -dependence of the scattering rate is superlinear, which is unlike the observed T -dependence that remains linear down to temperatures as low as $T = 40$ mK. This, along with an abnormally strong slope $\partial\rho/\partial T$, excludes electron-phonon scattering as a mechanism for the observed T -dependence.

The scattering mechanism due to electron-electron interaction in a Fermi liquid is expected to cause a T^2 -dependence, which extend from the lowest temperatures up to temperatures of the order of the bandwidth. The scattering rate is high due to the uniquely strong e-e interactions in graphene-based systems, and can be further enhanced by Umklapp scattering. The T^2 -scaling matches the observed T -dependent transport up to doping values near the edges

of the flat band, corresponding to a small concentration of electrons or holes. However, it is distinct from the strong linear T dependence $\rho(T)$ observed throughout most of the flat-band range in doping.

These general conclusions are illustrated below for a simple model of a flat band chosen to match the MATBG crystal symmetry and bandwidth, for realistic values of the e-e and e-ph interaction strength.

The scattering mechanism which, according to the reported transport measurements, appears to be at work in MATBG at low temperatures is unique for the **quantum-critical systems**. The properties of the ground state in these systems are dominated by soft modes which are strongly coupled to carriers and produce a T -linear scaling of resistivity. This is indeed the scaling observed in MATBG at low temperatures and in a wide range of carrier concentrations. The T -linear resistivity was first linked to strong-coupling superconductivity when the high-temperature cuprate superconductors were discovered. Subsequently, T -linear resistivity has been seen in the pnictide and organic superconductors, as well as in many heavy fermion compounds, both superconducting and non-superconducting. In most of the heavy fermion materials, the T -linear resistivity is seen when they have been tuned by some external parameter to create a low-temperature continuous phase transition known as a quantum critical point. The T -linear resistivity is therefore often associated with quantum criticality [14].

Theoretical models explaining the T -linear resistivity typically rely on carrier scattering by strongly fluctuating degrees of freedom such as gauge fields [15] or the fluctuations due to the critical soft modes [16]. While presently there is no single universally accepted explanation for the T -linear resistivity, it is understood to be a universal property of many strongly-interacting electron systems. The high scattering rate associated with the T -linear resistivity is sometimes called "Planckian dissipation", referring to the fact that the scattering rate per kelvin is well approximated by the ratio of the Boltzmann constant to the Planck constant divided by 2π (e.g. see Ref.[14]). These values are consistent with those found in the measurements described in the main text.

A. Resistivity due to electron-phonon scattering

Electron-phonon scattering is often the dominant contribution to the resistivity in metals, in which case the resistivity shows a $\rho \propto T^1$ behavior at $k_B T \gtrsim T_{BG}/4$ whereas $\rho \propto T^4$ at the lower temperatures. This is also likely to be the case for MATBG [45], but with a smaller energy scale than in typical metals. A recent study also points out that the resistivity shows $\rho \propto T^2$ at a very high temperature where the temperature is comparable or larger than the bandwidth [46], if the nearly-flat band is well separated from the other high-energy bands. To gain ideas on the window of temperature for T -linear resistivity by electron-phonon interaction, we have calculated the phonon resistivity using the honeycomb lattice model coupled to acoustic phonons. To see the typical temperatures where the two crossovers takes place, we consider a honeycomb lattice model coupled to acoustic phonons. The electron Hamiltonian reads

$$H_e = \sum_{\vec{k}} \begin{pmatrix} \psi_{\vec{k},1}^\dagger \\ \psi_{\vec{k},2}^\dagger \end{pmatrix}^T \begin{pmatrix} 0 & h_{\vec{k}} \\ h_{\vec{k}}^* & 0 \end{pmatrix} \begin{pmatrix} \psi_{\vec{k},1} \\ \psi_{\vec{k},2} \end{pmatrix}. \quad (1)$$

Here $h_{\vec{k}} = t \left(1 + e^{-i\vec{k} \cdot \vec{a}_1} + e^{-i\vec{k} \cdot \vec{a}_2} \right)$ with t the nearest-neighbor hopping, $\vec{a}_{1,2} = a \left(\pm \frac{1}{2}, \frac{\sqrt{3}}{2} \right)$, $|\vec{a}_{1,2}| = a$, are primitive vectors and $\vec{k} = (k_x, k_y)$ is electron momentum. The phonon Hamiltonian

reads

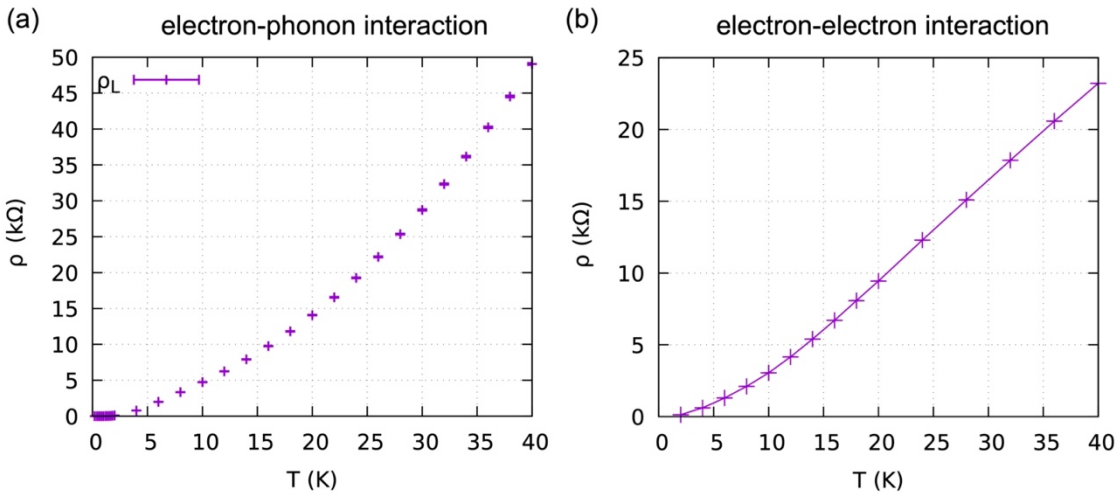
$$H_p = \sum_{\vec{q}} \hbar \omega_{\vec{q}} \hat{a}_{\vec{q}}^\dagger \hat{a}_{\vec{q}}, \quad \omega_{\vec{q}} = s |\vec{q}|, \quad (2)$$

where $\hbar \omega_{\vec{q}}$ is the energy of the phonon with momentum \vec{q} and the sum over \vec{q} runs over the momenta \vec{q} in the SL Brillouin zone. Recent study of phonons in moiré graphene finds a dispersion that, at low energies, is similar to that of the monolayer graphene [47,48]. Therefore, we use the sound velocity $s = 1.5 \times 10^4 \text{ ms}^{-1}$, a typical value observed in graphene [47,48]. The electrons and phonons interact through deformation coupling,

$$H_{ep} = - \sum_{\vec{q}, \vec{k}, n} \frac{g_{\vec{q}}}{\sqrt{V}} \sqrt{\hbar \omega_{\vec{q}}} \hat{\psi}_{\vec{k}, n}^\dagger \hat{\psi}_{\vec{k}, n} (\hat{a}_{\vec{q}} + \hat{a}_{-\vec{q}}^\dagger). \quad (3)$$

Here, $V = \sqrt{3}a^2 N/2$ is the area of the system, N is the number of the SL unit cells, and $g_{\vec{q}} = g e^{-q^2 \xi^2/4}$ is the form factor where ξ is a parameter reflecting the Wannier function radius; this formfactor, with $\xi = 1/5 - 1/6$, reproduces that of the Wannier function of TBG [46].

The resistivity $\rho(T)$ of a system is related to entropy production. We use the variational method assuming the conventional form of the field-induced modulation of electron distribution $\delta f_{n\vec{k}} = f_{n\vec{k}} - f_{n\vec{k}}^0 = \tau e \vec{E} \cdot \vec{v}_{n\vec{k}} \beta f_{n\vec{k}}^0 (1 - f_{n\vec{k}}^0)$, where $f_{n\vec{k}}$ and $f_{n\vec{k}}^0$ are respectively the electron occupation rate and Fermi distribution for electrons on n th band and momentum \vec{k} . within this method, the



Supplementary Figure S 6. Temperature dependence of the resistivity for MATBG at $\theta = 1.12^\circ$. (a) The phonon resistivity for the sound velocity $s = 1.5 \times 10^4 \text{ ms}^{-1}$, orbital radius $\xi = a/6\sqrt{3}$ (see the form factor below Eq. 3 for details; a is the lattice parameter) and $g^2 = 9.37 \text{ eV}\text{\AA}^2$, which corresponds to the deformation potential $D = 20 \text{ eV}$ [23] and mass density $1.52 \times 10^{-10} \text{ kg cm}^{-2}$. (b) The resistivity due to electron-electron scattering for $v/a^2 = 1.5 \text{ meV}$. In both figures, we used the bandwidth $W = 3t = 3.9 \text{ meV}$, the lattice parameter $a = 12.8 \text{ nm}$, and the filling $\nu = 2/3$.

resistivity reads [49]

$$\rho(T) = \frac{\sum_{n,n'} \int \frac{dk^2}{(2\pi)^2} \frac{dk'^2}{(2\pi)^2} \beta P_{n\vec{k},\vec{k}'-\vec{k};n'\vec{k}'}^{(\text{e-ph})} \left(v_{n\vec{k}}^x - v_{n'\vec{k}'}^x \right)^2}{\left[e \sum_n \int \frac{dk^2}{(2\pi)^2} (v_{n\vec{k}}^x)^2 \beta f_{n\vec{k}}^0 (1 - f_{n\vec{k}}^0) \right]^2}, \quad (4)$$

where

$$P_{n\vec{k},\vec{q};n'\vec{k}'}^{(\text{e-ph})} = 2\pi \delta_{n,n'} |g_{\vec{q}}|^2 \omega_{\vec{q}} N_{\vec{q}} f_{n\vec{k}}^0 (1 - f_{n'\vec{k}'}^0) \delta(\varepsilon_{n\vec{k}} + \hbar\omega_{\vec{q}} - \varepsilon_{n'\vec{k}'}) \delta(\varepsilon_{n\vec{k}} + \hbar\omega_{\vec{q}} - \varepsilon_{n'\vec{k}'}) \quad (5)$$

Here, $\varepsilon_{\vec{k}s} = s|h_{\vec{k}}|$ and $v_{\vec{k}s}^x = \partial_{k_x} \varepsilon_{\vec{k}s} / \hbar$ are respectively the eigenenergy and the group velocity of electron state with momentum \vec{k} and band index s , $\beta = 1/T$ is the inverse temperature, \vec{E} is the external electric field, and τ is the variational parameter. Figure S6.b shows the result of resistivity by electron-phonon scattering. The linear- T resistivity appears at around $T \sim 10$ K. However, the temperature dependence becomes super-linear at $T \lesssim 5$ K, as expected from the typical behavior of phonon resistivity in metals. The resistivity also deviates from a T -linear dependence at $T \gtrsim 30$ K due to the narrow bandwidth. The narrow window of T -linear resistivity cannot account for our experiment, in which the T -linear resistivity appears from $T \sim 20$ K down to $T = 40$ mK.

Besides the conventional acoustic-phonon contribution [45], other works point out a larger contributions from gauge phonon [50] and umklapp scattering [46]. The gauge-phonon contribution, however, shows a trend qualitatively similar to the acoustic phonons; it is $\rho \propto T^1$ in a wide range of temperature around $T \sim T_{BG}$, whereas they are nonlinear in the low temperature $T/T_{BG} \ll 1$. The umklapp scattering contribution become dominant at temperatures $T \gtrsim T_{BG}$ while their contribution is negligible in the low temperature. Hence, we conclude that the electron-phonon scattering cannot account for the T -linear resistivity down to 20 mK, even considering the contribution of unconventional scattering mechanisms.

B. Resistivity due to electron-electron scattering

We next turn to the resistivity by electron-electron scattering. In metals, the contribution from electron-electron interaction is often very small due to small umklapp scattering and their temperature dependence is $\rho \propto T^2$. To confirm the above behavior, we performed the calculation of resistivity using the variational method used for resistivity by electron-phonon interaction. The resistivity reads

$$\rho_{\text{int}}(T) = \frac{1}{4k_B T e^2} \frac{\sum_{s_i} \int \prod_i \frac{dk_i^2}{(2\pi)^2} Q_{\vec{k}_1 s_1, \vec{k}_3 s_3; \vec{k}_2 s_2, \vec{k}_4 s_4}^{(\text{int})} \left[v_{\vec{k}_1 s_1}^x + v_{\vec{k}_3 s_3}^x - v_{\vec{k}_2 s_2}^x - v_{\vec{k}_4 s_4}^x \right]^2}{\left\{ \int \frac{dk^2}{(2\pi)^2} (v_{\vec{k}s}^x)^2 \frac{\partial f_{\vec{k}s}^0}{\partial \varepsilon_{\vec{k}s}} \right\}^2}. \quad (6)$$

$$Q_{\vec{k}_1 s_1, \vec{k}_3 s_3; \vec{k}_2 s_2, \vec{k}_4 s_4}^{(\text{int})} = \frac{(2\pi)^3}{\hbar} \left(\frac{U_{\vec{k}_1 - \vec{k}_2}}{4} \right)^2 \frac{1 + s_1 s_2 s_3 s_4 \cos[s_1 \phi_{\vec{k}_1} - s_2 \phi_{\vec{k}_2} + s_3 \phi_{\vec{k}_3} - s_4 \phi_{\vec{k}_4}]}{2} \times f_{\vec{k}_1 s_1}^0 f_{\vec{k}_3 s_3}^0 (1 - f_{\vec{k}_2 s_2}^0) (1 - f_{\vec{k}_4 s_4}^0) \delta(\vec{k}_1 + \vec{k}_3 - \vec{k}_2 - \vec{k}_4) \delta(\varepsilon_{\vec{k}_1 s_1} + \varepsilon_{\vec{k}_3 s_3} - \varepsilon_{\vec{k}_2 s_2} - \varepsilon_{\vec{k}_4 s_4}). \quad (7)$$

Here, \vec{G} is the reciprocal lattice vectors, \hbar is the Dirac constant, and $U_{\vec{q}}$ is the Fourier transform of electron-electron interaction. For simplicity, we approximate the momentum dependence of scattering rate by $v^2 = (U_{\vec{q}}/4)^2$. Note that this resistivity is the usual contribution purely coming from electron-electron interaction, and not those from the non-Mathiessen contribution; the latter contribution appears in the presence of both impurity and electron-electron scatterings giving T^2 temperature dependence at a very low temperature. Figure S6.a shows the temperature dependence of the resistivity for electron-electron scattering, which shows a nonlinear curve below $T \lesssim 20$ K. The nonlinear temperature dependence is consistent with the common notion that the temperature dependence is $\rho \propto T^2$ when electron-electron scattering dominates. However, the calculated result is qualitatively different from what observed in our experiment, excluding the possibility of conventional electron-electron scattering mechanism.